

Supporting Information

Identifying the Origin of Thermal Modulation of Exchange Bias in MnPS₃/Fe₃GeTe₂ van der Waals Heterostructures

Aravind Puthirath Balan^{1‡*}, Aditya Kumar^{1‡}, Patrick Reiser³, Joseph Vimal Vas⁴, Thibaud Denneulin⁴, Khoa Dang Lee⁹, Tom G Saunderson^{1,10}, Märta Tschudin³, Clement Pellet-Mary³, Debarghya Dutta³, Carolin Schrader³, Tanja Scholz⁵, Jaco Geuchies⁷, Shuai Fu⁷, Hai Wang⁷, Alberta Bonanni⁶, Bettina V. Lotsch⁵, Ulrich Nowak⁸, Gerhard Jakob¹, Jacob Gayles⁹, Andras Kovacs⁴, Rafal E. Dunin-Borkowski⁴, Patrick Maletinsky^{3*}, Mathias Kläui^{1,2*}

[‡]These authors contributed equally

* Correspondence to aravindputhirath@uni-mainz.de, patrick.maletinsky@unibas.ch, klaeui@uni-mainz.de

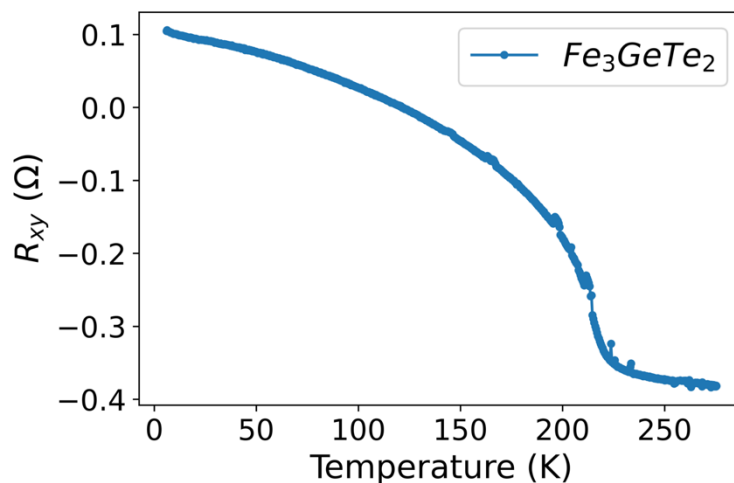
SI1. Magnetic Characteristics of Fe₃GeTe₂ exfoliated flakes

Figure S1. Anomalous Hall resistance (R_{xy}) measured as a function of temperature for an exfoliated Fe₃GeTe₂ flake

The anomalous Hall effect resistance plotted as a function of temperature at 100 mT field applied out-of-the-plane for a similar Fe₃GeTe₂ flake utilized in this study is given in **Figure S1**. Additionally, we extensively discuss the anomalous Hall effect (AHE) hysteresis observed in a Fe₃GeTe₂ flake of comparable thickness, obtained from the identical bulk crystal utilized in the present investigation, in our recently published work about bulk spin-orbit torques in Fe₃GeTe₂ [F. Martin et al., *Materials Research Letters* **2023**, 11, 84–89].

SI2. The spin Hall magnetoresistance signal of an MnPS₃/Pt device

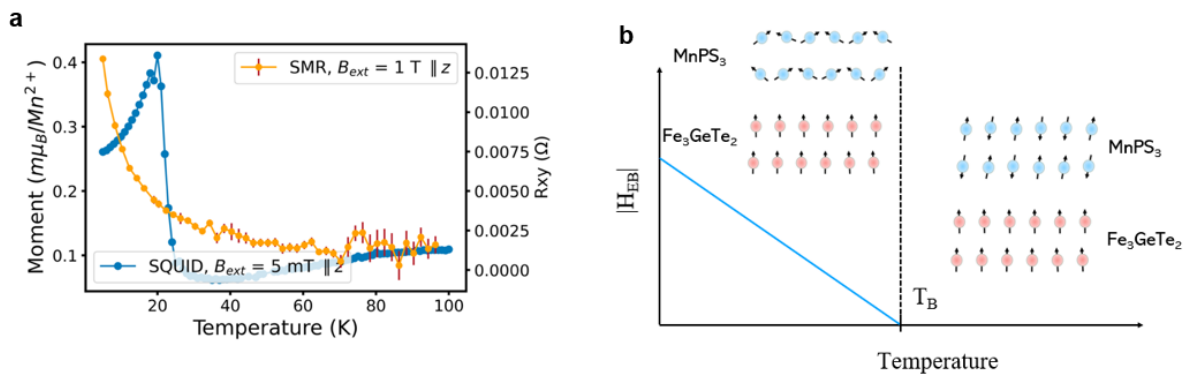


Figure S2 a) Spin-Hall magnetoresistance (SMR) of MnPS₃/Pt device measured as a function of temperature exhibits a rise below 40 K similar to that observed in bulk MnPS₃ crystal M vs. T curve suggesting the emergence of weak FM order. b) Schematic showing an intuitive model of exchange bias occurring below 40 K. The anomalous ferromagnetic moment observed in SQUID and NV magnetometry measured in MnPS₃ confirms this spin-reorientation transition below 40 K which induces exchange bias in Fe₃GeTe₂.

Temperature dependence of spin hall magnetoresistance in MnPS₃/Pt device was measured and is shown in **Figure S2**. The increase in V_{xy} below 40 K also confirms the emergence of ferromagnetic order in exfoliated MnPS₃ flakes at lower temperatures.

SI3. Field dependence of the uncompensated Moment of MnPS₃

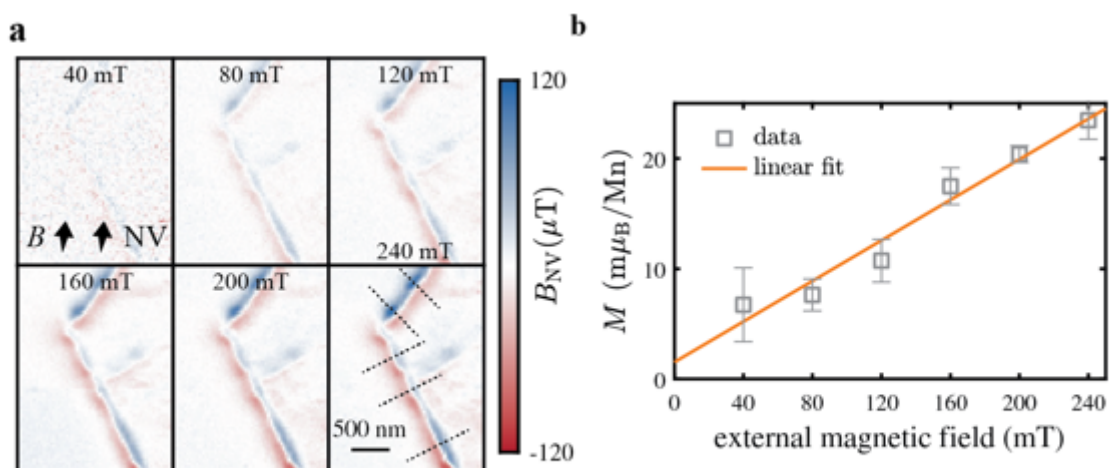


Figure S3. a) Consecutive images obtained from the isolated MnPS₃ flake at various applied magnetic fields along the NV axis, as indicated by the arrows. The dotted lines in the image acquired at $B_{ext} = 240$ mT indicate the position for the linecuts used to estimate the signal strength. **b)** Signal strength as estimated from the linecuts shown in **a**. Depicted uncertainties indicate the standard deviation between the linecuts. The axis has been normalized by the magnetization obtained from the linecut shown in Fig. 3. A linear function is fitted through the data points.

Figure S3 provides a comprehensive analysis of the field dependence of the uncompensated moment of MnPS₃, shedding light on its magnetic behavior under varying external conditions. Figure S1a presents a series of consecutive images showcasing the isolated MnPS₃ flake under the influence of different applied magnetic fields along the NV axis, as indicated by arrows. Notably, in the image acquired at an external magnetic field strength of $B_{ext} = 240$ mT, dotted lines demarcate the positions for the subsequent linecuts employed for signal strength estimation. The corresponding results are illustrated in **Figure S3b**. The uncertainties associated with the measurements are denoted by error bars, representing the standard deviation observed between the various linecuts. To provide a normalized perspective, the axis has been scaled by the magnetization acquired from the linecut exhibited in **Figure S3a**, ensuring a consistent basis for comparison. Intriguingly, a linear function has been fitted through the data points, offering a mathematical description of the observed relationship between the applied magnetic field and the resulting signal strength.

SI4. Hysteresis cycle of the uncompensated moment of MnPS₃ flake

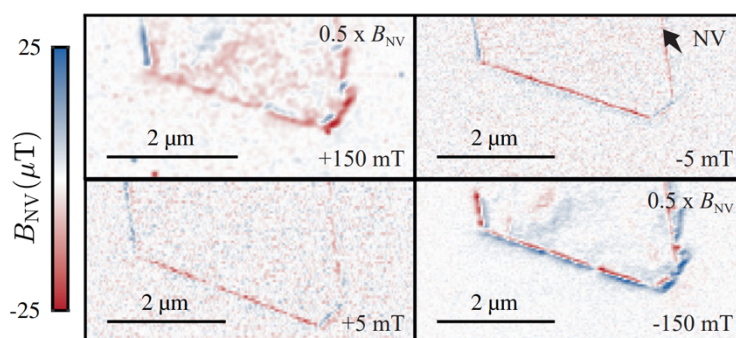


Figure S4. Consecutive images were obtained from the isolated MnPS₃ flake at various applied magnetic fields along the NV axis, as indicated by the arrow. The applied field follows the hysteresis cycle $B = +150 \text{ mT} \rightarrow -5 \text{ mT} \rightarrow -150 \text{ mT} \rightarrow +5 \text{ mT}$. Interestingly, though the magnetization switched at $\pm 150 \text{ mT}$, the polarity of the remanent magnetization at $\pm 5 \text{ mT}$ remains unchanged contrary to the SQUID data obtained from a bulk crystal.

Figure S4 summarizes consecutive images derived from an isolated MnPS₃ flake that were acquired while subjecting it to varying applied magnetic fields along the NV axis, as depicted by the directional arrow. The magnetic field applied to the system followed a hysteresis cycle, specifically transitioning through the values of $B = +150 \text{ mT}, -5 \text{ mT}, -150 \text{ mT},$ and $+5 \text{ mT}$. Notably, an intriguing observation emerged during the analysis, wherein the magnetization exhibited a switch in polarity at magnetic field strengths of $\pm 150 \text{ mT}$. However, in stark contrast to the SQUID (Superconducting Quantum Interference Device) data obtained from a bulk crystal, the remanent magnetization at $\pm 5 \text{ mT}$ retained its polarity, remaining unaltered throughout the cyclic magnetic field perturbation. This unexpected behavior highlights a distinctive aspect of the MnPS₃ flake's magnetic response, deviating from the anticipated trends observed in bulk crystal counterparts. The findings underscore the importance of investigating nanoscale structures for a comprehensive understanding of magnetic properties and their potential implications for applications in nanotechnology and spintronics.

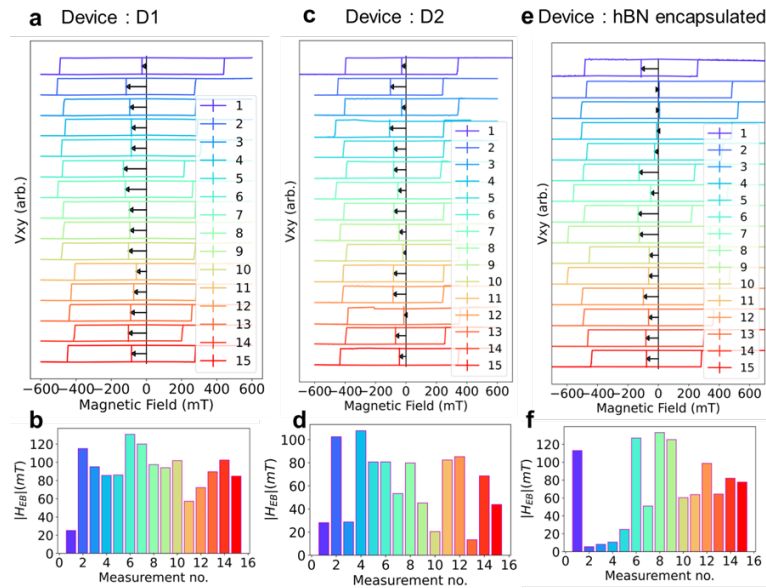
SI5. Thermal cycling induced metamorphosis of exchange bias in MnPS₃/ Fe₃GeTe₂

Figure S5. The top row shows AHE hysteresis plots, and the bottom row summarizes the magnitude of measured exchange bias after each of the 15 consecutive cycles. **a)** and **b)** h-BN/MnPS₃/Fe₃GeTe₂ sample (D1). **c)** and **d)** h-BN/MnPS₃/Fe₃GeTe₂ sample (D2) to confirm reproducibility of evolving exchange bias. **e)** and **f)** h-BN/MnPS₃/Fe₃GeTe₂/h-BN sample (D3). This device is fabricated and measured to check the effect of stress from substrate clamping on Fe₃GeTe₂ flake due to a mismatch in the thermal expansion coefficient of Fe₃GeTe₂ and Si/SiO₂ substrate. However, no significant difference is observed in exchange bias evolution in D3 compared to devices D1 and D2.

Figure S5 illustrates the dynamic metamorphosis of exchange bias in MnPS₃/ Fe₃GeTe₂ van der Waals (vdW) heterostructures induced by thermal cycling. The top row presents anomalous Hall effect (AHE) hysteresis plots, while the bottom row summarizes the measured magnitude of exchange bias after each of the 15 consecutive thermal cycles. The figure is organized into distinct panels, each corresponding to a different heterostructure configuration. **Figures S5a** and **b** showcase the results obtained from the h-BN-capped MnPS₃/Fe₃GeTe₂ sample (D1). These panels provide AHE hysteresis plots and document the evolving magnitude of exchange bias across the thermal cycles. Similarly, **Figures S5c** and **d** present results from a second h-BN capped MnPS₃/Fe₃GeTe₂ sample (D2), confirming the reproducibility of the observed evolution in exchange bias.

To investigate the influence of substrate clamping-induced stress on Fe_3GeTe_2 flake on the dynamic evolution of exchange bias, a device is fabricated with an h-BN encapsulation instead of capping. **Figures 5d and e** depict results obtained for the h-BN encapsulated $\text{MnPS}_3/\text{Fe}_3\text{GeTe}_2$ sample (D3). Considering the mismatch in the thermal expansion coefficient between Fe_3GeTe_2 and the Si/SiO₂ substrate, it's possible that roughness in the substrate can clamp the vdW FM Fe_3GeTe_2 and induce a net non-zero stress in device D1 and D2. Remarkably, substrate clamping has no significant influence on the evolution of exchange bias, suggesting that the dynamic evolution of exchange bias depends solely on the thermal cycling induced modification of the $\text{MnPS}_3/\text{Fe}_3\text{GeTe}_2$ interface registry. Plotting the histogram of exchange bias in these measurements in **Figure S4** does not show a particular type of distribution and there is no correlation observed among the three devices. A larger number of measurements may be required to give any conclusion about the nature of the distribution and if there any correlation.

SI6. The distribution of exchange bias in $\text{Fe}_3\text{GeTe}_2/\text{MnPS}_3$ vdW heterostructures

The distribution of exchange bias for D1, D2 and D3 during 15 consecutive cycles are summarised in **Figure S6**. It is evident that the distributions are not identical due to limited number of iterations.

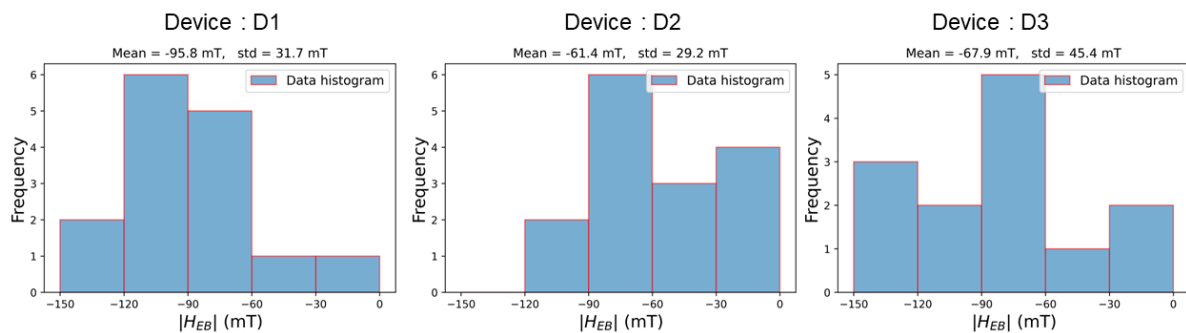


Figure S6. The mean of distribution for 15 measurements for D1, D2, and D3 is -96 mT, -61 mT, and -68 mT respectively. The standard deviation of distribution for the three devices is 32 mT, 29 mT and 45 mT respectively.

SI7. Cross-sectional STEM sample preparation

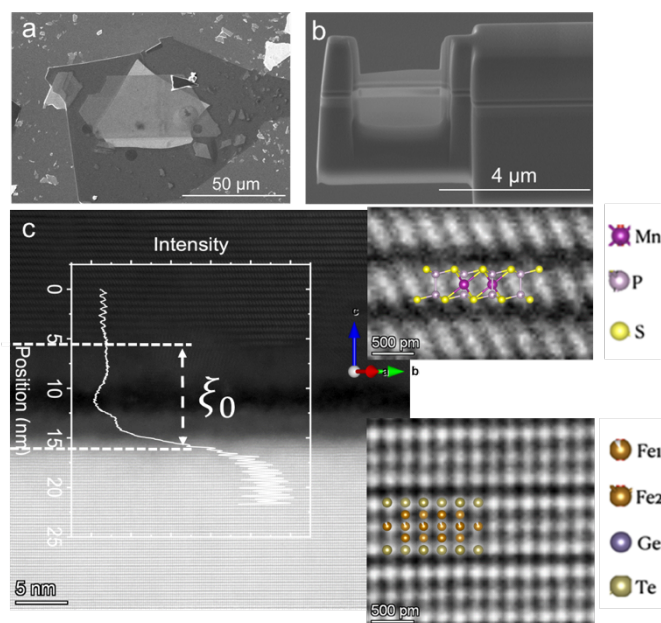


Figure S7. a) Scanning electron microscope image of h-BN/MnPS₃/Fe₃GeTe₂ stack, b) Cross-sectional lamella on a typical STEM grid, and c) Cross-sectional STEM of the stack with the inter-crystalline distance (ξ) indicated. HAADF (high angle annular dark field) images of the crystalline regions are shown in the insets with colour-coded atomic positions.

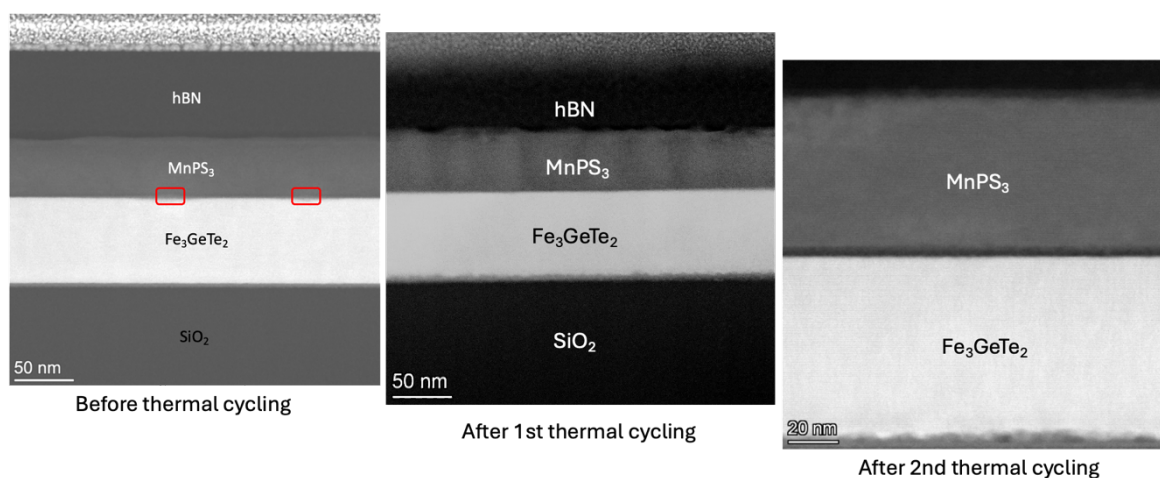
SI8. Low resolution cross-sectional STEM of the MnPS₃/Fe₃GeTe₂ interface

Figure S8. The images shows that the intercrystalline distance remains consistently uniform across the cross-section except for small variations of the gap at certain regions (indicated in red rectangles). The

presented value for the intercrystalline distance in the manuscript is averaged over different images acquired for a cross-section with standard deviation indicated.

SI9. Cross-sectional STEM EDX of the MnPS₃/Fe₃GeTe₂ interface

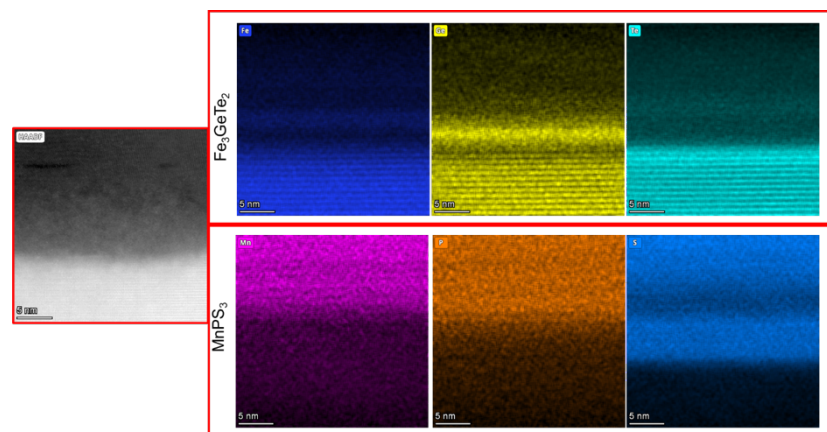


Figure S9. Elemental mapping images acquired through STEM EDX reveal the migration of elements across the vdW gap. Particularly noteworthy is the translocation of sulfur from MnPS₃ layers proximate to the interface to the corresponding layers of Fe₃GeTe₂. This results in the formation of amorphous layers that act as a separator between the crystalline regions on either side of the vdW gap.

SI10. Total energy dependence of the MnPS₃/Fe₃GeTe₂ interface from first principles

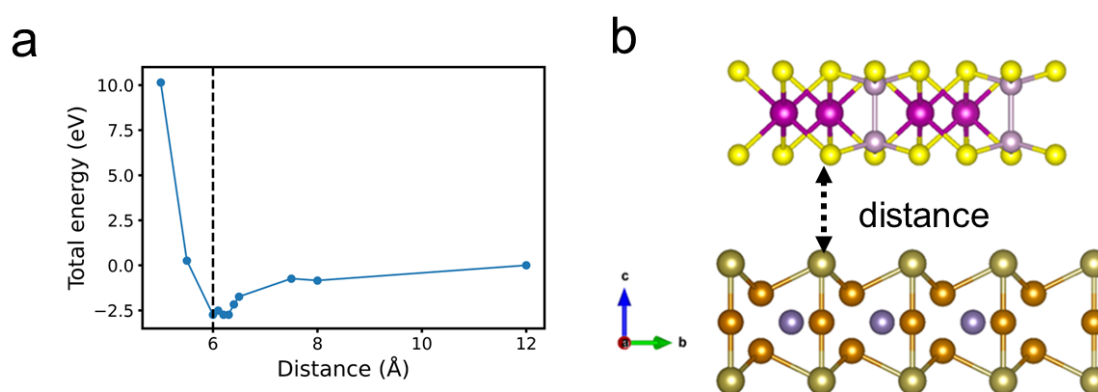


Figure S10. First-principles calculations using the Density Functional Theory code VASP were performed for different vdW distances of Fe₃GeTe₂ and MnPS₃. (a) shows the total energy which becomes unstable below 6 angstroms. (b) shows the Fe₃GeTe₂ and MnPS₃ stack used in the calculation.

SI11. Structural characterizations of the materials and their heterostructures

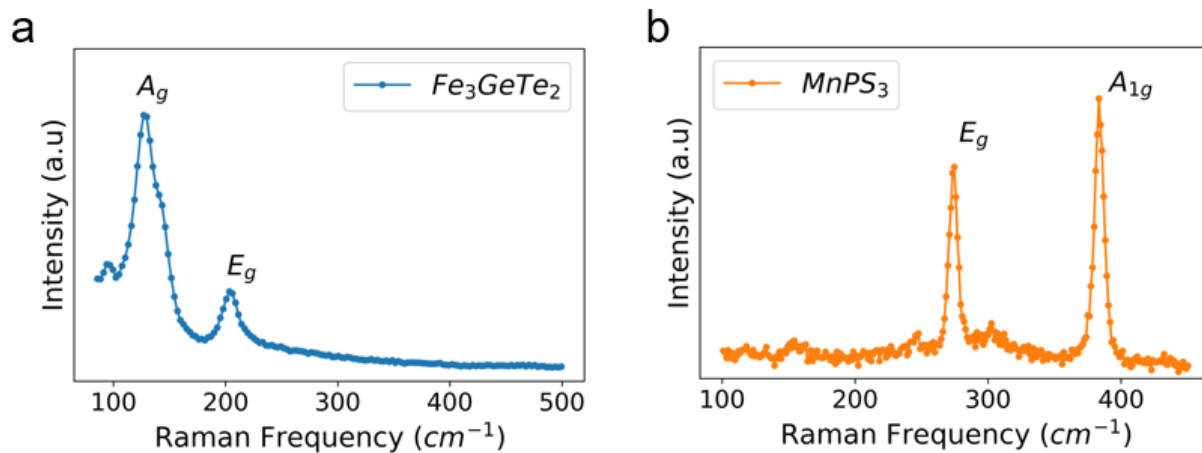


Figure S11. Raman spectroscopy of Fe_3GeTe_2 and MnPS_3 crystals used for fabricating devices in this work.

SI12. Atomic force microscopy analysis of device 1 (D1)

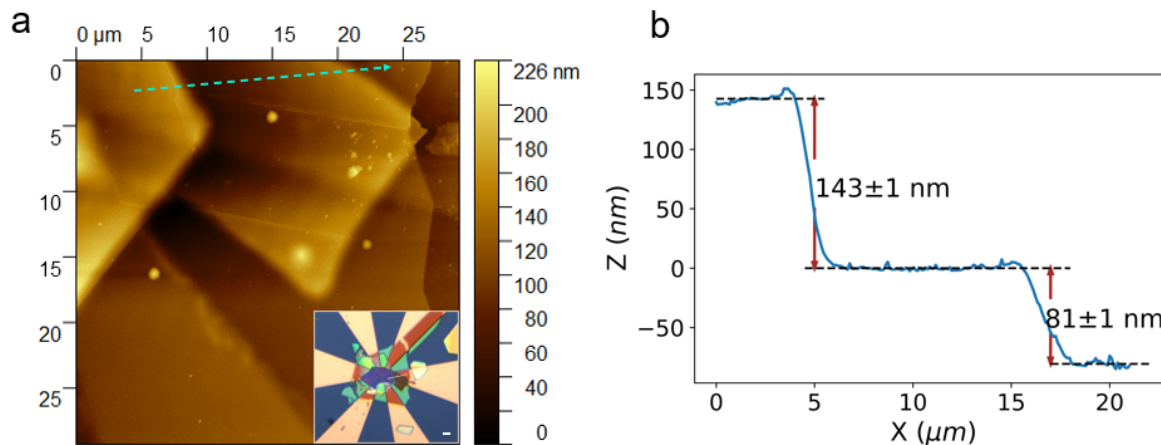


Figure S12. a) atomic force microscopy image: the green dashed line shows the line used to calculate thickness. The inset shows an optical image of the sample. b) The linecut shows the thickness of the Fe_3GeTe_2 layer to be close to 80 nm and the MnPS_3 flake to be close to 140 nm.